THE JOURNAL OF PHYSICAL CHEMISTRY C

Article

Cite This: J. Phys. Chem. C 2019, 123, 9298−9310

pubs.acs.org/JPCC

Intermetallic Differences at CdS−Metal (Ni, Pd, Pt, and Au) Interfaces: From Single-Atom to Subnanometer Metal Clusters

S. S. Gupta and M. A. van Huis*

Soft Condensed Matter, Debye Institute for Nanomaterials Science, Utrecht University, Princetonplein 5, 3584 CC Utrecht, The Netherlands

Supporting Information

ABSTRACT: Metal co-catalysts tipped at a photocatalyst surface form a crucial component in the nanoheterostructures designed for the photocatalytic hydrogen evolution reaction. To examine the intermetallic differences and size effects at these interfaces, we use spin-polarized density functional theory to study single-atom, 13-atom, and 55-atom cluster depositions of Ni, Pd, Pt, and Au on the CdS($10\bar{1}0$) surface. For the single metal atoms, the ground-state configuration was the same site for all of the elements. Analysis of the metal−CdS bonding and of the charge transfers revealed a Ni−Cd bonding complex leading to depletion of electronic charge at the Ni single atom and at deposited Ni clusters, in contrast to charge accumulation observed for the other three metals Pd, Pt, and Au. For scaling up sizes of the metal deposition, six subnanometer cluster types were selected over a wide range of cluster's effective coordination number, and their interfaces were differentiated by charge redistributions, structure and adhesion energies, highest occupied molecular orbital−lowest occupied molecular orbital (HOMO-LUMO) gaps, and Schottky barrier heights. Although all considered clusters are semiconducting in the gas phase, 9 out of 28 clusters became (semi)metallic after deposition on the CdS semiconductor surface. Intermetallic differences and common trends are discussed.

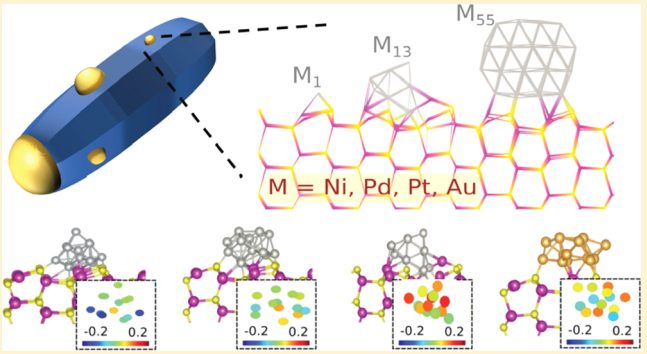

1. INTRODUCTION

Over the last decade, semiconductor nanoheterostructures have marked significant progress in the advent of photolysis of water, or more specifically, in its redox half-reactions.[1−3] These nanostructures often comprise of semiconductor−semiconductor and metal−semiconductor (M−Sc) interfaces, which serve as a sink for the electrons or holes photogenerated from the photocatalyst. The metal−semiconductor (M−Sc) interfaces play a central role in the underlying photoelectrochemistry of hydrogen evolution reactions, wherein the semiconductor is exploited for its photoexcitation properties and the transition metals for their excellent reducing and catalytic properties. Among these nanostructure designs, those based on CdS as the photocatalyst have emerged to be of importance owing to their promise of having suitable band edges, and overall superior photocatalytic efficiencies.[4,5] However, they exhibit a well-known shortcoming of photodegradation due to the accumulation of holes which pose a limiting challenge for the overall water-splitting. Second, current practice requires the use of sacrificial agents like methanol or sulfates to consume the photogenerated holes for carrying out the oxidation half-reaction.[1,3,6] Nevertheless, for their unprecedented efficiency in hydrogen evolution reaction,[2] they are one of the most often used components in photocatalytic nanoheterostructures.

Typically, noble and expensive metal co-catalysts are widely used to facilitate excellent electron transfer at the M−Sc interface, leading to higher catalytic activity than a bare photocatalyst.[7] In the pursuit of obtaining comparable yields at lower costs, non-noble metals or their alloys are often tested for their suitability of forming an efficient M−Sc interface. This requires an understanding of bonding peculiarities of different metals with the CdS photocatalyst. Keeping this question in view, we seamlessly examine intermetallic differences for the M−Sc interfaces of single-atom and subnanometer-sized metal clusters, for some widely used co-catalysts of 3d, 4d, and 5d metals (Ni, Pd, Pt, and Au). Further, the question of optimal size of the metal co-catalysts is still open, depending on factors like photocatalyst morphology and facet of co-catalyst deposition. Several studies have experimentally shown that subnanometer cluster sizes are optimal for catalytic performance,[8−11] while, on the contrary, a recent study has indicated much larger cluster sizes (∼5 nm) to be more suitable.[12] Deposition of clusters beyond nanometer dimensions is clearly beyond the current feasibility of spin-polarized ab initio modeling. Here, considering that the deposition of single-atom and subnanometer metal clusters can highlight intermetallic bonding differences at the M−Sc interfaces, we have studied a

Received: March 13, 2019
Published: March 20, 2019

DOI: 10.1021/acs.jpcc.9b02319
J. Phys. Chem. C 2019, 123, 9298−9310

range of cases for single-atom, 13-atom, and 55-atom cluster adhesions varying in their site of adhesion, compactness, and gas-phase stability.

While several studies have reported higher quantum yields where the metal depositions are at the polar CdS facets, it is challenging to model a realistic structure of a polar surface as they are known to undergo reconstructions to stabilize the built-in electric fields. A well-known example thereof is the ZnO polar surfaces, which have been studied over a decade to characterize the realistic reconstructions of the semiconductors' surface.[13,14] In experiments, the exposed facets of a nanoparticle are controlled in the growth process by exploiting the facet binding preferences of long-chain or short-chain organic ligands.[15,16] Here, as for the CdS substrate we choose the CdS $(10\bar{1}0)$ wurtzite facet, owing to its prominence in CdS nanostructures and structural tractability. There are also examples of using the $(10\bar{1}0)$ facet for metal deposition, for different CdS morphologies like rods,[9] platelets,[17] and tetrapods,[18] which have shown significant success.

In the colloidal environment, the type of cluster depositions is controlled by several factors like metal precursor concentration, oxidizing or reducing chemical species, laser exposure, and temperature.[3,10] To capture the variety of M−Sc interfaces possibly formed in such conditions, in our study, we have modeled a variety of M−Sc interfaces for each metal. We have included not only the most stable gas-phase clusters (from the literature) but also those which are likely to react strongly with the CdS surface. We use the criterion of effective coordination number (ECN),[19,20] which indicates the compactness or openness of clusters, also suitable for even distorted cluster geometries. In the recent literature, the coordination number of extended metal surfaces has been directly correlated with the free energy of adsorption at the surface,[21] hence proposing a systematic surface descriptor of catalytic activity. An extension of these findings to deposited clustered metal surfaces is not straightforward, as apart from surface curvatures, substrate-induced dipole effects are expected to have a direct effect on catalytic activity. In this work, we sample locally stable gas-phase clusters over a wide ECN range. Typically, these metals are known to be stabilized in either closed or open structure (i.e., with high-ECN or low-ECN, respectively). Using this intermetallic difference for Ni, Pd, Pt, and Au, we effectively sampled a set of clusters comprising both low-lying and high-lying isomers in their potential energy surfaces, which were deposited to characterize their M−Sc interfaces.

First, we begin by investigating the intermetallic differences for the single-atom adsorption of four metals in Section 3.1. In Section 3.2, we elucidate upon the gas-phase metal clusters reported in the literature, which are either the putative global minima (PGM) of a study or theoretically well-studied cases like icosahedron or two-dimensional metal sheets. This leads to a set of at least 10 isolated gas-phase clusters for 13-atom and 55-atom cases (i.e., diameters, ca. 0.5−1 nm), as shown in Figure S1 in the Supporting Information (SI). From this large set of clusters in Section 3.3, we further selected a set of six clusters for each metal, which represent a wide range in their respective effective coordination number (ECN) space and thus screen a variety of M−Sc interfaces.

2. METHOD AND SETTINGS

Density functional theory[22,23] calculations were performed with VASP,[24,25] using the basis set of all plane waves with kinetic energy less than 400 eV. The projector augmented-wave potential sets[26,27] were used for the ionic description, with a plane-wave cutoff of 580 eV for augmentation charges. The valence states included for all atoms are 3s3p for S, 3d4s for Ni, 4d5s for Pd and Cd, and 5d6s for Pt and Au. The many-body electron−electron interactions are approximated using the generalized gradient approximation (GGA) for the exchange-correlation functional Perdew−Burke−Ernzerhof (PBE).[28] For all of the calculations, spin-polarized density functional theory (DFT) was used as it is experimentally and theoretically known that in the subnanometer-size regime considered here, several of these metals exhibit magnetic moments due to either undercoordination of surface atoms or exchange splitting near the Fermi level.

2.1. CdS $(10\bar{1}0)$ Surface. Studying clusters of subnanometer sizes requires the use of sufficiently large supercells to counter adjacent image interactions. In constructing the $(10\bar{1}0)$ wurtzite CdS surface slabs, we have used the lattice constants of a = 4.15 Å and c = 6.75 Å, within 0.5% to the reported experimental values,[29,30] with a thickness of five bilayers (BL) and lateral dimensions of 20.7 × 20.2 Å^2. The bottommost slab layer was passivated by pseudohydrogens with nuclear charges Z_{H-Cd} = 1.5 and Z_{H-S} = 0.5, to facilitate smoother band edges and a bulklike termination for the surface. The 5BL passivated surface used for single-atom, 13-atom, and 55-atom clustered depositions comprises 330 atoms. In Figure S1 in the SI, a surface unit slab of 5BL thickness is shown to be sufficiently large to depict surface and subsurface states in comparison to a 16BL unpassivated slab. For the convergence of total energy for clean CdS and deposited cases, we used a Gaussian smearing scheme with a width of 0.05 eV. Dipole corrections were added[31,32] to cancel the dipoles resulting from the asymmetric adsorption on the slab model, thus preventing the interaction between the dipoles of the neighboring cells. The criterion for electronic convergence was 10^{-5} eV, while the atoms in the cell were relaxed until the forces reduced to 0.01 eV/Å.

The semiconductor's fundamental band gap as well its band edge positions are important in studying M−Sc's electronic structure. It was earlier believed that the most of the band gap error of standard DFT functionals occurs at the conduction band minima (CBM), and consequently, the theoretical studies estimated the n-type Schottky barrier heights (SBHs) using the experimental band gaps and theoretically derived valence band edge.[33] However, with increasing accuracy of many-body perturbation theory calculations, recent studies have reported this expectation to not hold, especially for II−VI semiconductors. Studies have shown that the bulk CBM predictions of PBE are already very good in comparison to GW calculations and that the error in band gap is mostly in predicting the valence band maxima (VBM).[34−37] Due to this, their surface CBM predictions (with respect to vacuum) using the standard GGA-PBE functional show excellent agreement with the spectroscopic measurements of electron affinity (EA).[34] This finding, although fortuitous for the PBE-level theory, has been exploited here to directly determine the n-type SBH, without using the PBE-predicted VBM. The 5BL passivated slab used in this work has EA = 4.58 eV ($EA_{exp.}^{(11\bar{2}0)}$ = 4.79 eV[38]) and a fundamental band gap of 1.33 eV ($BG_{exp.}$ = 2.55 eV[29]), indicating that the valence band edge of the slab bears most of the band gap error. This enables us to directly predict the n-type Schottky barrier heights (SBH) of the CdS−metal junctions. Our tests with the DFT + U scheme[39,40] have

DOI: 10.1021/acs.jpcc.9b02319
J. Phys. Chem. C 2019, 123, 9298−9310

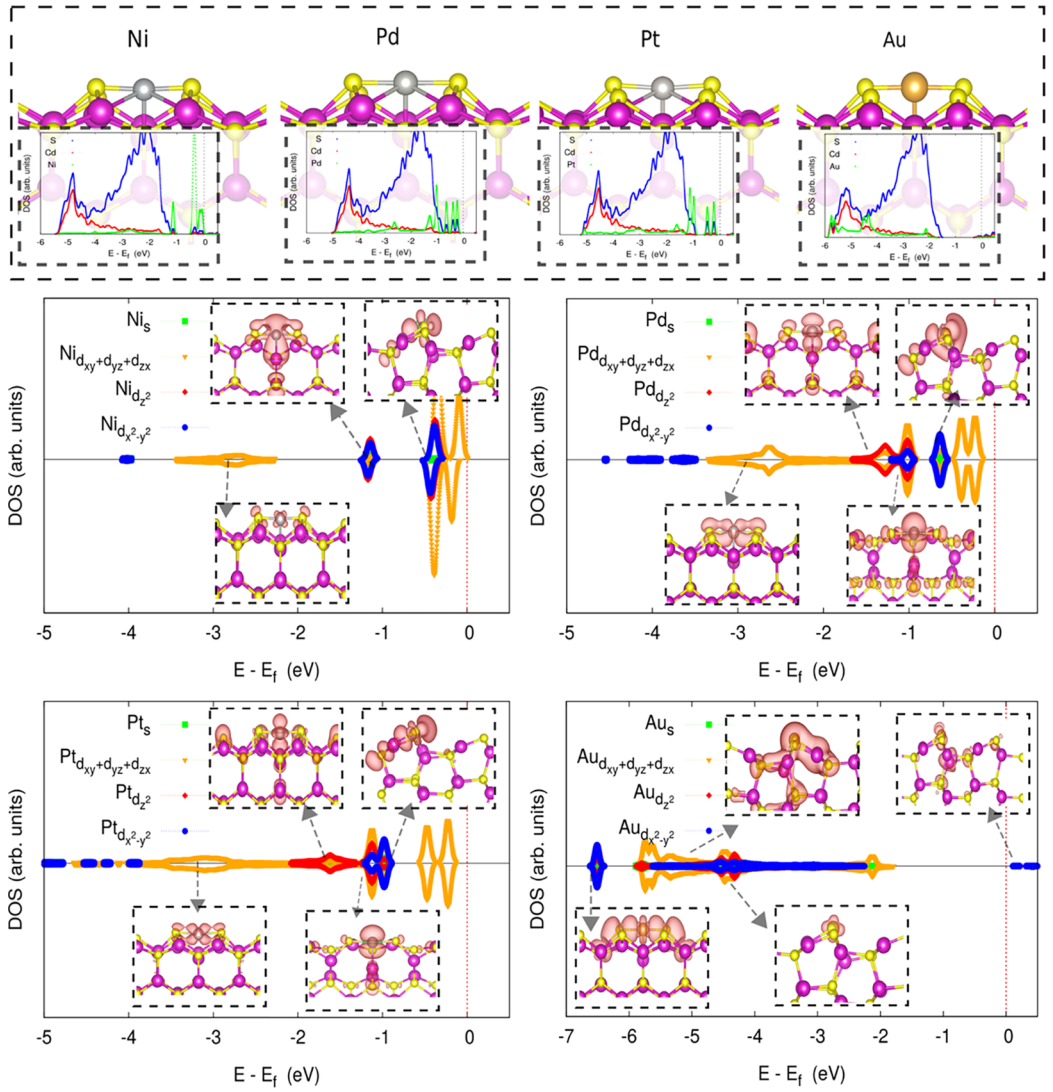

Figure 1. Top) Ground-state configuration of adsorbed metal single atoms. The insets represent the total density of states of the metal atom and those of the Cd and S atoms of the topmost slab layer. (Bottom) Projected density of states (PDOS) of each metal atom for their respective GS configuration shown above. The insets show the partial charge densities of the indicated states, for the isosurface value of 1×10^{-3} e/Å^3. Structure files of all configurations are available as Supporting Information.

shown that simultaneously correcting the surface band edges and the band gap is not attainable within reasonable U values. Hence, we have chosen standard DFT calculations over the DFT + U scheme to determine the n-type SBH in Section 3.4.

The lateral dimensions were successfully tested to be sufficiently large for obtaining the geometries of the adsorbed clusters (detailed in Section 3.3). The deposited metal atoms and clusters were relaxed using the Γ-point, for sampling the Brillouin zone. The calculations for density of states (DOS) were performed with 10 irreducible k-points, using a $4 \times 4 \times 1$ k-mesh. The total energy difference between the Γ-point calculation and the one with 10 irreducible k-points varies from 1 to 3 meV/atom depending on the metal and specific deposited case. Unless mentioned otherwise, the reported total energies are derived using the 10 irreducible k-points.

3. RESULTS

3.1. Single-Atom Adsorption. Studying the case of single-atom adsorption not only provides a limiting reference for understanding intermetallic differences for M−Sc interfaces, but it also holds relevance for the recent advances in the pursuit of single-atom catalysis.[41,42] For the single-atom, it is well known that an element's electronic configuration could be different from that of its bulk form. In agreement with the literature,[43] we find the ground-state (GS) electronic configurations of different metal atoms as: $3d^9 4s^1$ for Ni, $4d^{10} 5s^0$ for Pd, $5d^9 6s^1$ for Pt, and $5d^{10} 6s^1$ for Au. Their magnetic moments are 2, 0, 2, and 1 μ_B for Ni, Pd, Pt, and Au, respectively. For testing the adsorption of metal single atoms on CdS $(10\bar{1}0)$, we investigated for different sites in the [0001] and $[1\bar{2}10]$ lateral directions, which led us to the conclusion that the ground-state (GS) configuration for all of the metal atoms is the same site, as shown in the top panel of Figure 1. Three other locally stable configurations are shown in Figure S2. These configurations are referred to as GS-1, GS-2, and GS-3, which are defined by their adhesion energy differences, $\Delta E^i_{GS} = E^{GS\text{-}i}_{adh} - E^{GS}_{adh}$, from their respective GS configuration of Figure 1. In the GS configuration, the metal atom is between the $[1\bar{2}10]$ atomic rows, allowing a maximum number of metal−substrate bonds. The M−S bond length for

DOI: 10.1021/acs.jpcc.9b02319
J. Phys. Chem. C 2019, 123, 9298−9310

M = Pd, Pt, and Au is 2.3 Å (each within a deviation of 0.03 Å), and for Ni−S, it is 2.13 Å.

We will first discuss the surface bonding for the metal single atoms of the Ni group (Ni, Pd, and Pt). The magnetic moments for all of the four adsorbed cases of these metals are almost zero. The total density of states (DOS) for the surface Cd and S atoms and the adsorbed metal atom are shown in the insets of the top panel of Figure 1 (for GS) and Figure S2 (for metastable states). The states in the CdS band gap and near the valence band edge are the transition metal's d-orbitals. These can be clearly seen from the projected density of states of the metal atom in the bottom four panels of Figure 1 (for GS) and Figure S3 (for metastable states). To visualize the bonding of these states, the partial charge densities of some of the bonding orbitals formed by the metal atom and the CdS surface are shown as insets (isosurface = 1×10^{-3} e/Å^3). In general, the highest occupied states are antibonding orbitals comprising the d_{xy}, d_{yz}, and d_{zx} states, while the bonding orbitals are composed of two sets: the deeper ones (at ∼3 eV) with a relatively low density of states, comprising d_{xy}, d_{yz}, or d_{zx} orbitals, and the other at energies between 0 and 1.5 eV, comprising $d_{x^2-y^2}$ and d_{z^2} orbitals. The density of the deeper set of bonding states (at ∼3 eV) is small for Ni_1, and increases for Pt_1 and Pd_1. For the latter two, these states have a small bonding contribution with the two neighboring S atoms and a delocalized contribution over the surface anions. Second, in the higher set of bonding orbitals of $d_{x^2-y^2}$, d_{z^2} has a distinct surface-induced splitting depending on the metal atom. For Ni_1, these orbitals distinctly split into two types, where the deeper orbital (at ∼1.2 eV) forms a complex with the nearest Cd atom, while the other set (at ∼0.5 eV) weakly bonds with S atoms. The Ni−Cd bonding is noteworthy, as the Ni electron density is polarized toward the surface cation, which together participates as a complex with the neighboring S atoms. The d_{z^2} and $d_{x^2-y^2}$ orbitals in Pd_1 have a contribution to three states within ca. 0.5−1.3 eV. A correspondence with the Ni_1 case shows that the lower two of the three states (ca. 0.9−1.3 eV) have a weaker polarization in the direction of the nearest Cd atom, but a greater contribution in the direct bonding with the neighboring S atoms. The topmost of the bonding orbital shows an enhanced directional bonding with the S atom. Similar to Pd_1, the d_{z^2} and $d_{x^2-y^2}$ in Pt_1 split into a set of three bonding orbitals, with a broader spread in energy, between ca. 0.9 and 2 eV. In comparison to Pd_1, the deepest of the orbital has a lower density of states and more of a delocalized contribution than the bonding with the neighboring S atoms. The top two of the split bonding levels have a smaller energy difference than for Pd_1 and show no interaction with the nearest Cd atom, but instead exhibit a more directional interaction with S atoms, when going higher in energy. The analysis of the partial charge densities and the magnitude of projected density of states indicates that the tendency to locally bond with the nearest Cd cation decreases from Ni → Pd → Pt, while delocalized bonding with surface S has the trend Ni < Pd ∼ Pt, expectedly for intermetallic differences for 3d → 4d → 5d. For Au_1, the d-orbitals are much deeper in the valence band region of CdS. The deepest bonding orbital splits apart, comprising d_{z^2} and contributions from $d_{x^2-y^2}$ and s-orbitals, which bonds with the two neighboring S atoms. The higher states have a dispersed nature due to the relaxations on the surface caused by the large atomic radius of Au atom. The GS case of Au_1 has zero magnetic moment.

We will now discuss the three locally stable sites (GS-1, GS-2, and GS-3) for Ni_1, Pd_1, Pt_1, and Au_1 in Figure S2. The stability trend for metastable cases Ni_1 and Pd_1 exhibits the same order. Within a cutoff of 3.05 Å, the number of Ni−Cd and Pd−Cd bonds decrease from 3, 1, and 1 for GS-1, GS-2, and GS-3 configurations, respectively. The ordering of these metastable sites for Au is opposite to that of Ni and Pd. The Au−S bond lengths positively correlate with the configuration stability (given, all geometries provide only one Au−S bond). The Pt_1 locally stable geometries of Figure S7 are at least 1 eV less stable than the GS of Pt_1 shown in Figure 1. Each of these three geometries has one S−Pt bond in comparison to the two S−Pt bonds of the GS, indicating the stabilizing role of the deep Pt−S states in the bonding diagram. The configurational stability of the single-atom Pt cases does not exactly match with that of Au. Our ordering of preferred adsorption sites for a single Pt atom agrees with those reported in Xiong et al.[44] They had used the total dipole moments of the cell to infer the distribution of charge between metal and the substrate. This could be misleading due to spurious dipole cancellations and additions, especially when there are as many as five bonds with a single metal atom. Following this approach, they had inferred that the Pt_1 donates charge to the surface, while for Pt clusters, the electronic charge transfer seemed to be opposite (to the Pt clusters). In the sections below, we will show that the inferences from Bader charges give a consistent picture of charge transfers for single metal atom and their clusters.

The three locally stable cases of Ni group metal atoms also exhibit the localization/delocalization trends seen for their respective GS cases. The partial charge densities shown in Figure S3B highlight the bonding state, which forms a Cd complex in Ni_1, also compared to a similar state in the corresponding cases of Pd_1 and Pt_1. Clearly, the polarization toward Cd decreases from Ni → Pd and Pt, while the delocalization over surface S atoms is greater for Pd and Pt in comparison to Ni. The PDOS for metastable Au_1 cases has markedly two sets of orbitals: intact d-orbitals (at ca. 2.5−3 eV), which have a weak charge-induced bonding interaction with the surface, and an antibonding s-state near the Fermi level, which shows a contribution of a Au complex with the nearest Cd cation on the surface. The Au atom in isolated form has a magnetic moment of 1 μ_B, which remains same for all of the three locally stable cases in Figure S2. This difference between the GS of Au_1 and the three locally stable cases can be seen from their PDOS in Figures 1 and S3, where the latter cases have a state showing a prominent s-orbital character (close to Fermi level), which is hybridized in the GS case. The deepest bonding state in the GS case of Au_1 at ∼6.5 eV has a clear bonding orbital associated with Au−S, which is missing in the GS-1, GS-2, and GS-3 cases, thus explaining the stability of the GS of Au_1.

For identifying the metallic or semiconducting nature of the deposited surface, we studied the occupancies of KS orbitals, for 9−10 irreducible *k*-points, using a smaller Gaussian smearing width of 0.01 eV or tetrahedron smearing method.[45] The GS and metastable states for Ni_1, Pd_1, and Pt_1 cases are semiconducting, while the Au_1 ground state is metallic, where the conduction band closest to the Fermi energy has a varied occupancy over different *k*-points. This is interesting, as one expects semiconducting nature to prevail for the low coverage adsorption of single-atom case. The partial charge density that leads to this metallic contribution is shown in the Au_1 PDOS of Figure 1, where the conduction band edge has an enhanced

DOI: 10.1021/acs.jpcc.9b02319
J. Phys. Chem. C 2019, 123, 9298−9310

contribution at the displaced Cd atom and neighboring surface atoms. Here, the Au_1 PDOS is not seen to not cross the Fermi level as the semimetallic state is localized at the displaced CdS surface atoms and not at the Au atom. The three metastable Au_1 states do not cause significant surface distortions and are found to be semiconducting.

We also studied the GS and GS-1 configurations of Au_1 using a static, spin−orbit coupling (SOC) calculation. The PDOS for these are shown in Figure S5a,b (Supporting Information), to be compared with their respective cases with spin-polarized calculation in the Au_1 case of GS configuration shown Figure 1 and GS-1 of Au_1 configuration shown in the third column of Figure S3 (Supporting Information). First, in terms of the deep energy level at ∼6.5 eV, comparison suggests that the electronic difference between GS and GS-1 qualitatively remains the same for with or without SOC. Owing to the SOC effect, in comparison to the spin-polarized cases, we see fine splitting of the d-orbitals (at ca. 4−6 eV) of the Au_1 for both the configurations. This spitting is also seen for the s-orbitals near the Fermi edge, for the GS-1 case, resulting in semimetallic behavior like GS. This suggests that fine spitting in SOC can affect the metallicity of the interfaces, which we will also observe later for the cluster aggregates.

For determining charge transfers from/to the metal atom, we have used the Bader partitioning and integration scheme.[46] Figure 2 shows bar plots for difference in the Bader charges of

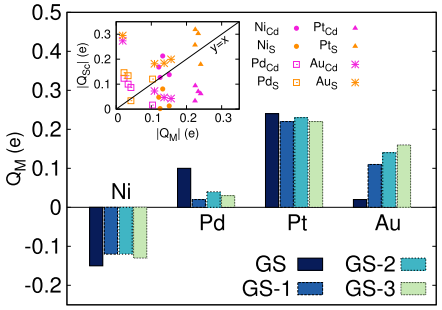

Figure 2. Bars in the main panel show the Bader charges, Q_M of metal atoms for all single-atom adsorptions over CdS $(10\bar{1}0)$. GS refers to the ground state with largest E_{adh}, and GS-i (i = 1−3) refers to the metal-stable sites with decreasing adhesion energy. The inset compares the absolute sum of Bader charges for the semiconductor ions ($|Q_{Sc}|$) with the absolute metal Bader charges for the respective cases.

the metal atoms (Q_M) with and without the CdS surface, for all of the adsorption sites. A positive value indicates the accumulation of charge at the metal atom. First, we see that Pd, Pt, and Au show accumulation of charge, while Ni shows depletion of charge for all configurations. In terms of charge transfer, Ni and Pt mark the two extremes among the four metals. Second, for Pd and Au, the charge transfer changes significantly upon changing the adsorption sites. In fact, their GS charge distribution is not representative of the flexibility in their bonding patterns. Unlike these, Ni and Pt show almost the same transferred charge for all of the four sites. This could be possible if they have a preferential interaction with either the anions or cations of the surface. To further examine this, we considered the sum of differences in Bader charges for all of the cations (Q_{Cd}) and all of the anions (Q_S) in the supercell, for each configuration, with and without the metal atom. Naturally, for all of the cases, we have $Q_M + Q_S + Q_{Cd} = 0$, within an accuracy of $10^{-3}e$. In the single-atom adsorption case, where surface reconstructions are minimal, one can assume that the ions with leading contributions to this sum should play a direct role in charge transfer with the metal atom. In the inset of Figure 2, we have plotted the absolute values of Q_{Cd} and Q_S as a function of the absolute value Q_M of the respective adsorption case. If the $|Q_{Cd}|$ or $|Q_S|$ is above the $y = x$ line ($y > x$) or close to it, then the bonding with that species is dominant in the total charge transfer of the metal atom. However, when the charges on anions and cations are opposite, both $|Q_{Cd}|$ or $|Q_S|$ could be in the $y > x$ region.

The inset of Figure 2 clearly indicates that the charge transfer from Ni is to the Cd atoms, and that to Pt occurs from the S atoms, as the Bader charges of these substrate atoms are relatively in the vicinity of the $y = x$ line (in comparison to the other surface species). These selective charge transfers are consistent with their nearly constant Bader charges in the bar charts. The effect of degree of localization of d-bands in the Ni atom was examined by using the DFT + U scheme for Ni atom, with U_{Ni} = 3.5 eV. Figure S4 shows that for DFT + U and PBE, Ni shows a depletion of Bader charge; however, the localization of d-states causes a reduction in charge depletion of ca. 0.03−0.07e. The GS for Pd_1 is dominated by transfer from S atom to Pd, while the other three geometries show a mixed share of metal bonding. For the GS case of Au_1, Q_{Au} = 0.02e, while Q_{Cd} and Q_S are 0.27e and −0.29e, respectively. This is due to the size of the Au atom and the large bond lengths it forms, which distorts the Cd−S bonds of the surface as highlighted earlier; thus, the signs of Q_{Cd} and Q_S are opposite and are affected by the surface distortions. In all other locally stable cases (GS-1, GS-2, and GS-3), Au exhibits charge transfer from the surface S atoms.

In the subsequent sections, we will shift our focus onto the interfaces made by aggregates of metal atoms. The metal aggregates considered are at least 10 known gas-phase clusters of different metals, structurally characterized by their ECN; thereafter, for a select few of the metal clusters, we report their relaxed depositions over the CdS $(10\bar{1}0)$.

3.2. Gas-Phase Clusters.

$$d^i_{avg} = \frac{\sum_j d_{ij} \exp\left[1 - \left(\frac{d_{ij}}{d^i_{avg}}\right)^6\right]}{\sum_j \exp\left[1 - \left(\frac{d_{ij}}{d^i_{avg}}\right)^6\right]} \quad (1)$$

$$\mathrm{ECN}_i = \sum_j d_{ij} \exp\left[1 - \left(\frac{d_{ij}}{d^i_{avg}}\right)^6\right] \quad (2)$$

$$d_{avg} = \sum_i d^i_{avg}/N \quad (3)$$

$$\mathrm{ECN} = \sum_i \mathrm{ECN}_i/N \quad (4)$$

Generally, the studies on gas-phase metal clusters focus on searching for the putative global minima (PGM) within the scope of their search algorithms and the representative physical theory. However, for studying realistic interfaces made by metal clusters, both the depositions made by PGM clusters and metastable cluster candidates become interesting. The structure of a deposited cluster would be kinetically driven

DOI: 10.1021/acs.jpcc.9b02319
J. Phys. Chem. C 2019, 123, 9298−9310

by several factors at the interfacial site. To account for this, we choose to study weakly and strongly reacting cluster candidates within ground-state DFT, instead of simulating these clusters within a classical or an ab initio molecular dynamics approach.

It is well known that the metal clusters in these metals show a typical stability preference for either ordered/compact or disordered/open structures.[20,47−50] Going from 3d to 5d metals, the localization of d-bands decreases, leading to more open and distorted structures.[51] This openness/compactness of a cluster is well captured using the concept of a cluster's effective coordination number (ECN).[19,20] Thus, sampling across a wide ECN enables a systematic sampling of high and low-lying cluster geometries. In this work, the ECN is derived from eqs 1 to 4, as in the cluster literature.[19,20] Equation 1 describes the average bond distance for an atom, d^i_{avg}, which is self-consistently obtained using a weighted sum of all its bond pairs, d_{ij} (and not just an atom's neighborhood). This was solved for the convergence criteria of $d^i_{avg}(\text{new}) - d^i_{avg}(\text{old}) \leq 0.0001$. By including all bond pairs within a cluster, ECN is expected to be a reasonable descriptor for coordination number of disordered clusters.

The clusters that we adopted from the gas-phase metal cluster literature of Ni, Pd, Pt, and Au[20,48,49,52−56] are shown in Figure S6, spanning from ECN = ca. 4−8.5. The clusters are sorted by an increasing ECN (from left to right). We relaxed these 13-atom and 55-atom clusters within the same computational settings as mentioned in Section 2, but with a smaller Gaussian width of 0.01 eV, within a box of at least 20 A^3. These gas-phase clusters can be classified into three types: (i) reported putative global minima from the literature, for Ni, Pd, Pt, and Au; (ii) theoretically well-studied cases of face-centered cubic (FCC) precursors like icosahedral and cuboctahedral; and (iii) the reported low-lying structures of one element, which were then used for the other three elements. FCC fragment for Pd_{55},[49] planar structure for Au_{13},[48] and distorted reduced core (DRC)-type structure for Au_{55}[49] and Cd_{55}[56] are such examples.

Figure 3 shows the stability preferences of different metal clusters by plotting their absolute binding energy (|BE|) as a function of their ECN. The inset in Figure 3 shows the same as a function of cluster's d_{avg}, which is numerically calculated using eq 1. In the main panel, when moving from left to right, the data points represent 13-atom and 55-atom clusters. On the extreme right (ECN ∼ 12), the data points represent respective metal's bulk BEs. As we cover only the cluster of subnanometer size, which is understood to be in the nonscalable regime of matter, one expects that any one parameter like ECN or d_{avg} cannot strictly determine stability. However, general stability preferences for a particular metal can be clearly drawn from Figure 3. In agreement to gas-phase cluster literature, it is seen that Ni and Pd stabilize toward higher-ECN geometries (i.e., more compact) than Pt and Au, which prefer lower-ECN geometries (i.e., more open). This is clearly observed for the most stable metal clusters, where $ECN_{Ni} > ECN_{Pd} > ECN_{Pt} > ECN_{Au}$. This is understood as the 3d and 4d-bands are more localized to the atomic core than the 5d-bands, leading to a more rigid and compact interatomic bonding. This fundamental signature of the metal bonding is also seen, where the d_{avg} of the most stable metal clusters inter-relate in the same order as their bulk counterparts, such as $d^{Ni}_{avg} > d^{Pd}_{avg} > d^{Pt}_{avg} > d^{Au}_{avg}$.

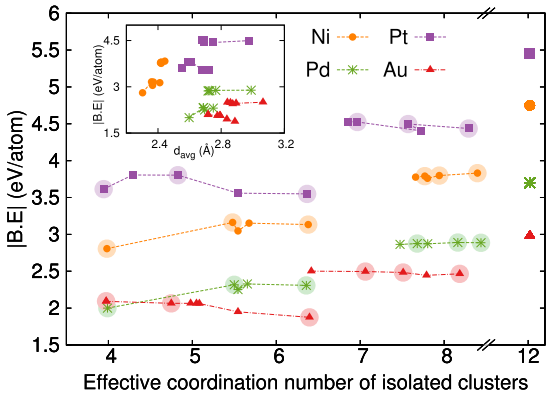

Figure 3. Graph showing the absolute gas-phase binding energies (|BE|) plotted as a function of their ECN for metal clusters in Figure S2, adopted from the literature. The data points on the left and right correspond to 13-atom and 55-atom clusters, respectively. The isolated data point on the extreme right is for the corresponding bulk binding energies. The inset shows the binding energies as a function of d_{avg}. The clusters chosen for deposition on the CdS surface are highlighted by circles.

For we have heavier elements like Pt and Au in our study, we have examined the effects of a full relativistic calculation by including spin−orbit coupling (SOC) effects. To benchmark the SOC effects, we have relaxed all of the isolated Au clusters within a full relativistic treatment. The results are shown in Figure S8a, where although the binding energies for SOC calculations are higher by ∼300 meV/atom, the overall trends of relative cluster stability do not alter. In agreement with a previous study,[20] we find that the geometry of the Au clusters does not significantly change, and the ECN and d_{avg} of the SOC-relaxed geometries and the PBE geometries fit well on the $y = x$ line. However, an intriguing case is found for the compact Au-icosahedral$_{13}$ (Au-ICO_{13}), where depending on the geometric optimization algorithm used, we found that the cluster geometry could remarkably alter to take a more open form with the SOC effect. Within the quasi-Newtonian algorithm, which specializes to find a local minimum, a metastable state with icosahedral symmetry was found to use standard spin-polarized settings. Figure S8b,c shows the differences in PDOS of a spin-polarized and an SOC cluster, for the ICO_{13} geometry. This could be expected since Au generally stabilizes to form open structures, while icosahedral is the most compact of the structural geometries considered here. This difference in stability of Au-ICO_{13} with and without including SOC is also evident in the highest occupied molecular orbital−lowest unoccupied molecular orbital (HOMO−LUMO) gaps for the two cases in Table 1. However, as most clusters do not significantly alter geometry, within the scope of this study, we will consider SOC to have no significant effect on the cluster's geometry. For the deposited cases, we will later discuss on single-point calculations for the Au clusters.

From the large set of gas-phase clusters shown in Figure S6, a selection up to at least six cluster types was chosen for each metal so as to study their respective interface with the CdS substrate. These selected sets are distinctly highlighted in Figure 3 with circles. Their relaxed geometries are shown in Figure 4 in the order of increasing ECN, and is composed of three 13-atom clusters (planar, icosahedron, and one of the stable reported geometries) and three 55-atom clusters (an open, intermediately open FCC fragment and a compact icosahedral cluster). Apart from covering a wide range of ECN,

DOI: 10.1021/acs.jpcc.9b02319
J. Phys. Chem. C 2019, 123, 9298−9310

Table 1. HOMO−LUMO Gaps (meV) of Selected Gas-Phase Clusters, for the Spin Channel Having the Smaller Gap[a]

cluster	Ni	Pd	Pt	Au
PLA	41	52	107 (133)	524 (124)
GS	140	58	183 (130)	155 (109)
ICO_{13}	75	69	149 (39)	1031 (48)
CCD	**6**	20	48 (26)	175 (26)
FCC	**3**	16	46 (36)	179 (52)
ICO_{55}	29	**0**	32 (67)	116 (31)

[a]For the 5d elements, the numbers in parentheses are the gaps corresponding to a single-point SOC calculation. The entries marked in bold highlight the cases having a gap smaller than 15 meV.

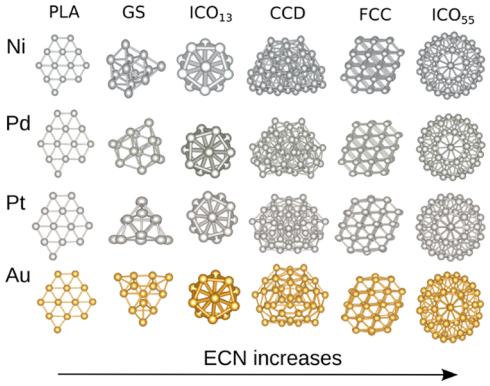

Figure 4. From left to right: set of 13-atom and 55-atom clusters deposited over CdS (10$\bar{1}$0) in the increasing order of effective coordination number (ECN).

our objective in choosing clusters for deposition was to select candidates which allowed some interesting features to be probed. The interest in these cluster types is detailed below, where we refer to the clusters using the shorthand nomenclature assigned in Figure 4. From left to right: (a) PLA—the two-dimensional, planar clusters are extraordinarily stable for Au up to a cluster size of 11,[52,57] unlike other transition elements. Reportedly, for Pd, Ni, and Pt, the 2D−3D transition occurs at $N \sim 4$.[50,58−60] Even for these relatively small clusters, atomicity theoretical studies have shown some differences in predicting their energy ordering near the PGM, owing to their differences in the exchange-correlational functional, basis sets, and accuracy of other numerical settings. This discussion is well covered in the cluster literature.[61,62] The reason for such high value of 2D−3D crossover for Au was earlier attributed to the SOC effects;[63] however, recent studies have also highlighted the bias of exchange-correlation functionals like GGA-PBE (both including and not including SOC) toward the planar structures.[50,52,61] Nevertheless, while PLA is a low-lying isomer for Au, it is a high-lying one for other elements. The clusters are expected to undergo 2D−3D makeover over the support, thus indicating the growth of a planar cluster of metal. (b) GS13—these structures are most stable (or are close to the PGM total energy) in freestanding form, and are adsorbed to identify the effect of stability of a metal on the nature of the M−Sc interface. For low-lying and interesting geometries, we choose a rhombohedral-like pyramid for Ni,[48] a biplanar geometry for Pd,[53] a trigonal pyramid geometry for Pt,[54] and a biplanar geometry for Au.[52] (c) ICO_{13}—icosahedral clusters have been considered for a large number of theoretical cluster studies as they are the most stable cluster geometries for noble gases and one of the precursors to form FCC crystals. It also marks the upper limit of effective coordination number, for 13-atom and 55-atom cluster sizes. (d) CCD—the distorted reduced core (DRC)-type structures[64] mark the low-ECN limit of 55-atom clusters and are reported to be the PGMs for Pt_{55} and Au_{55}.[20,49] However, we have chosen CCD, which in addition to having a low ECN also has a broad surface area to interact with the support. The CCD was reported for a Cd_{55} cluster reported using a Gupta potential.[56] It is similar to an oblate blob of atoms, which makes it a suitable choice. (e) FCC—this cluster is an FCC fragment and makes it a unique case to examine these metals, which crystallize into an FCC crystal in their bulk phases. Also, it is in the intermediate ECN range of 55 atoms. (f) ICO_{55}—lastly, we choose the high limit of ECN for the 55-atom cluster i.e., an icosahedral cluster.

In examining this selected set of six clusters in more depth, we report their magnetizations and HOMO−LUMO gaps. Figure S7 shows the spin densities of the selected six metal clusters along with their overall magnetic moments. In general, the cluster magnetic moments decrease from Ni → Pd → Pt → Au. It also shows that Pd, being isoelectronic to Ni, shows spin polarization throughout the cluster. In contrast to this, the spin polarization density in Pt_{55} and Au_{55} clusters could be either throughout the cluster (e.g., ICO_{13} and ICO_{55}) or localized at the surface of the clusters. In some cases, the atoms in Pt clusters also show opposite spin (colored blue), depending on the nature of exchange splitting. The (semi)metallicity of a metal cluster can been characterized by its HOMO−LUMO gap. In a spin-polarized calculation, there are two such gaps for each spin channel. In Table 2, we have reported the HOMO−LUMO gaps (in meV) of the spin channel with the smaller of the two gaps, to highlight how close these clusters are to attaining metallicity. First, for all metals, the increase in the atomicity of clusters from 13 to 55 atoms leads to broadening of bands, resulting in smaller gaps. Second, from an intermetallic comparison of five common clusters (PLA, ICO_{13}, CCD, FCC, and ICO_{55}), it is observed that the

Table 2. HOMO−LUMO Gaps of the Deposited Clusters (in meV), for the Spin Channel with the Smallest Gap[a]

clusters	Ni	Pd	Pt	Au	Au_{SOC}
HOMO−LUMO gap (in meV)					
PLA	101	232	165	**M**	**8**
GS	19	79	167	320	69
ICO_{13Pd}	114	67	28	385	**0**
ICO_{13Pt}	84	87	29	653	**9**
CCD	**8**	**0**	53	**M**	**M**
FCC	**8**	**13**	20	**M**	**M**
ICO_{55}	**12**	**4**	54	**M**	**M**
SBH (in eV)					
CCD	0.20	0.17		0.19	0.19
FCC	**0.08**	0.32		0.29	0.28
ICO_{55}	0.18	0.21		0.18	0.19

[a]The case having HOMO−LUMO gaps smaller than 15 meV are marked in bold and considered almost metallic (M). Respective values for the single-point SOC calculations for deposited Au clusters are also shown in the last column. The bottom table shows the SBH for the deposited cluster interfaces (in eV).

DOI: 10.1021/acs.jpcc.9b02319
J. Phys. Chem. C 2019, 123, 9298−9310

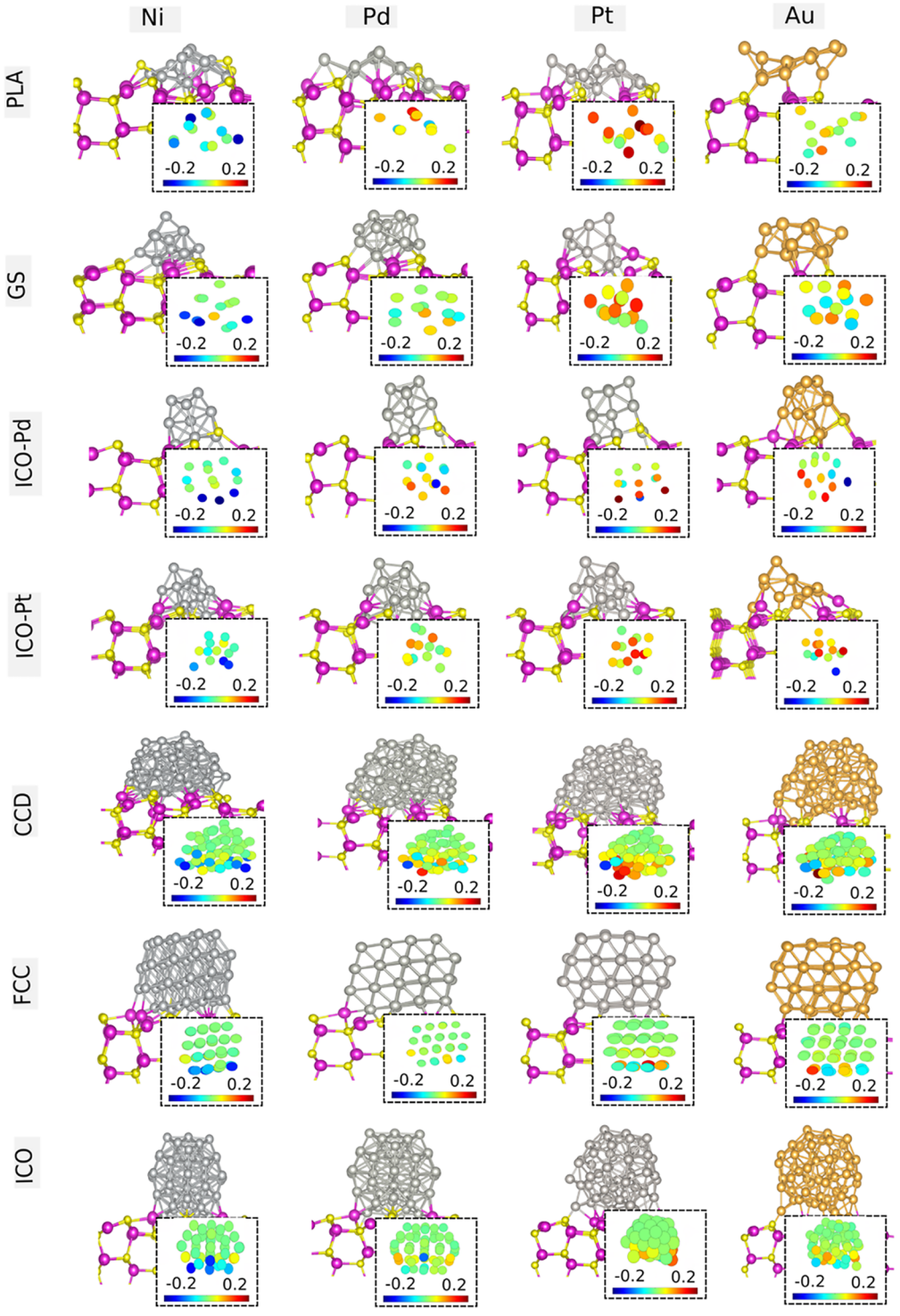

Figure 5. Relaxed geometries of deposited 13-atom and 55-atom clusters for Ni, Pd, Pt, and Au, on top of the CdS$(10\bar{1}0)$ surface. The index on the right indicates the shorthand names of the clusters deposited in this study. The inset explicitly gives a colormap representation of Bader charge difference of the metal atoms, which is coded with a scale indicating a range of ±0.25 electrons. Structure files of all configurations are available as Supporting Information.

HOMO−LUMO gaps increase from Ni → Pd → Pt → Au. Some of the 55-atom Ni and Pd clusters have gaps less than 15 meV, and can be considered almost metallic. SOC (given in parentheses) generally has the effect of reducing the HOMO−LUMO gaps.

3.3. 13-Atom and 55-Atom Depositions. The input geometries for depositing these clusters were selected so as to allow maximum interaction with the substrate. This was done by orienting the cluster such that the facet with a relatively large surface area is exposed to the CdS $(10\bar{1}0)$. For most of the cluster depositions (except ICO_{13} and CCD), we have used the metal cluster in their respective gas-phase geometry as an input for deposition. For the two cases of ICO_{13} and CCD, we have considered relaxed deposited geometries of one of the

DOI: 10.1021/acs.jpcc.9b02319
J. Phys. Chem. C 2019, 123, 9298−9310

metals as an input for corresponding calculations of the other metals. Such cases facilitate an intermetallic comparison as their relaxed geometries are very similar. We will elaborate on these below. To verify whether our simulation cells are sufficient in size for the deposition of clusters, for a selection of two 55-atom cluster geometries (Pt-CCD and Pt-ICO), we have relaxed the deposited geometries within a larger supercell of 24.8 × 26.9 Å^2, comprising 528 slab atoms. For a Γ-point calculation, the maximum change in adhesion energies was 1.6 meV/atom for Pt-CCD, which is expected since the surface stresses induced due to the cluster's large interfacial area would decrease in the larger cell. The geometries do not undergo any significant change. Hence, we would consider even our 55-atom clusters to be sufficiently converged in their relaxed geometries.

Now, with the understanding of intermetallic differences seen for the single-atom adsorption and knowing the characteristics of the metal clusters in the gas phase, we will report and discuss the interfaces formed by 13-/55-atom selected metal clusters with the CdS $(10\bar{1}0)$ surface. The relaxed cluster deposited geometries of the six selected clusters of each metal are shown in Figure 5. The inset of Figure 5 shows the colormap for Bader charge differences of the deposited metal cluster with and without the CdS surface. It is calculated by a simple difference of Bader charges from two single-point calculations of a deposited cluster and a freestanding cluster as in the deposited configuration. The color ranges from ±0.25 electrons. The Ni atoms close to the interface are blue, indicating a depletion of electrons, whereas many of the Pt atoms are colored orange or red (i.e., accumulation of electrons). The Pd and Au coloring is intermediate of these two extreme cases. This trend is qualitatively seen for all of the deposited clusters, which is also in agreement with the single-atom adsorption results.

The geometries are discussed below in the increasing order of cluster's ECN, starting with the PLA cluster deposition. Due to the reasons mentioned in Section 3.2, one expects the PLA for Ni, Pd, and Pt to strongly react with the surface and Au-PLA to have relatively weak interaction. Our observations of the relaxed geometries are concurrent with this expectation, which can be seen in Figure 5 for the row of PLA clusters. The Pd-PLA and Pt-PLA deposited cluster geometries tend to be similar to the Ni-PLA, where the cluster strongly reacts at the interface and a few S atoms are driven out of the surface to form clear metal−S bonds. In agreement with the expectation, Au-PLA shows a marked contrast with the PLA clusters of the other three metals, and is seen to maintain the planar network of the cluster by shifting away from the surface.

For Ni-PLA, we had adsorbed a stretched geometry of Ni-PLA (with larger lattice constant), where the interatomic distances in their input geometry were enlarged from their equilibrium distances. The interface geometry resulting from this initial cluster geometry is shown in Figure S9, Supporting Information. Ni chemisorbs to the surface, making a compact structure, which is partially bilayered and displaces the S atoms off the surface to form direct Ni−Cd and Ni−S bonds. The Ni−Cd complex observed for the single-atom adsorption was verified for these two Ni-PLA clusters. In Figure 6, the partial charge densities of one of the bands near the valence band edges are shown for the Ni-PLA geometries in Figures 5 and S9, Supporting Information. The arrows indicate the Ni−Cd complexes at the interface, in similarity with the single-atom cases.

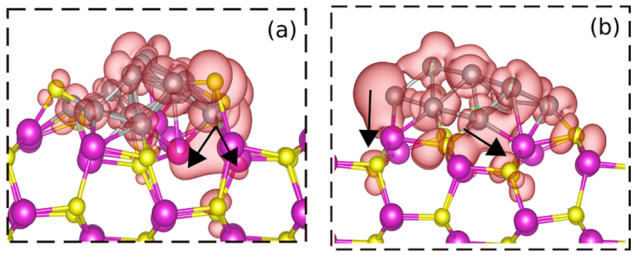

Figure 6. Partial charge densities of one of the bands close to the valence band edge show the Ni−Cd bonding complex, for two Ni-PLA geometries.

Second, the GS clusters are the low-lying clusters of the gas phase, which are practically different for all of the metals. The deposited geometries in Figure 5 show that the GS clusters mostly remain intact in their pyramidal or biplanar form, owing to their relative gas-phase stability. The Au-GS, similar to Au-PLA, results in minimal distortions in the CdS top layer.

Third, high-ECN 13-atom ICO clusters are very stable for Ni and Pd, while being very reactive for Pt and Au. Owing to this, one would expect large distortions and intermetallic variations within their relaxed deposited geometries if freestanding cluster geometry is used as an input. To enable a simpler intermetallic comparison for 13-atom ICO, we have used the relaxed geometries of Pd-ICO and Pt-ICO, as an input for all of the other three metals. Due to their differences in their gas-phase stability, the two types of cluster interfaces (called ICO_{Pd} and ICO_{Pt}) are quite different. Pt-ICO leads to a more distorted geometry than the compact Pd-ICO. In this manner, we have two types of depositions for each metal's ICO cluster, ICO-Pd and ICO-Pt, as shown in Figure 5.

First among the 55-atom clusters is the low-ECN CCD55. The broad basal surface area of this cluster is unique among the deposited cluster set. Like ICO13, in this case again, for a suitable intermetallic comparison, the inputs for CCD55 depositions for all metals were initiated from a relaxed Pt-CCD55 configuration (shown in Figure 5). After deposition, Ni-CCD55 and Pd-CCD55 reduce in size owing to their tendency to prefer compactness, while the Au-CCD55 transforms into a more open geometry. Second is the FCC fragment cluster, FCC55, which was the PGM for freestanding 55-atom Pd clusters.[49,64] As all of the four metals crystallize in FCC crystal structure, it is interesting to study how the FCC55 interacts with the surface. We have used the geometry reported by Piotrowski et al.[49] for Pd-FCC55. FCC55 freestanding geometries were used, in the same orientation, for deposition over the substrate. Third is the most compact, high-ECN ICO55 cluster. It is also the most stable geometry for Ni_{55}, a low-lying cluster for Pd_{55}, with a binding energy that is only 4 meV per atom lower in comparison to Pd-FCC55. The deposited cases of Ni-ICO55 and Pd-ICO55 remain compact and do not prefer to disperse on the surface like Pt and Au cases do. We observe this difference when we compare their geometries initiated from Pt-ICO55 and the geometries initiated from the freestanding ICO55 cases of respective metals. Figure S10 (Supporting Information) shows the less stable depositions derived from dispersed Pt-ICO55 cases. The geometries derived from the freestanding cases, which are compact and less dispersed, are 4.2 and 1.9 eV more stable for Ni and Pd, respectively.

3.3.1. Bader Charges. Using a colormap for the deposited clusters, the insets of Figure 5 qualitatively highlighted the

DOI: 10.1021/acs.jpcc.9b02319
J. Phys. Chem. C 2019, 123, 9298−9310

Bader charge difference, $Q_M(i)$, for every metal atom i. We have also plotted $Q_M(i)$ as a function of the z-coordinate of the atom i of the deposited cluster, in Figure S11. The orange line indicates the z-coordinate of the CdS surface before depositing the clusters. It is clear that these Bader charge differences reduce to almost zero within ~5 Å from the interface. Within intermetallic comparison, Pt_{13} and Pt_{55} clusters show the cases of maximum transferred charge. For Ni_{13} and Ni_{55} clusters, net charge is transferred to the surface from the Ni atoms. However, there are atoms in the Ni clusters, mostly in the subsurface layers near the interface, which gain electrons due to the induced dipoles in the clusters. Further, we summed the Bader charge differences of all of the atoms in the cluster ($Q_M = \sum Q_M(i)$), to estimate the overall charge transferred between the cluster and the CdS surface. In Figure 7, Q_M is shown as a bar plot for all of the deposited clusters. We observe that the charge transferred for 13-atom clusters is often comparable to that of 55-atom clusters, as it is primarily determined by the chemical bonding at the interface and the number of interacting atoms. For all metals, the cluster with the highest charge transfer is the CCD, having the advantage of its broad interfacial area. Similarly, in the 13-atom regime, the low-ECN clusters of Ni-PLA, Pd-PLA, and Pt-PLA show considerably higher charge transfer, in agreement with their stronger chemisorption and wider interfacial area. The overall charge transfer for clusters is about 5−10 times than the single-atom cases of Figure 2. The magnitudes $|Q_M|$ for Ni, Pd, and Au are comparable, while Pt shows markedly higher charges for each cluster case. The inset of Figure 7 shows Q_{Cd} and Q_S as mentioned in Section 3.1. The charge on the Cd atoms for the Ni cases (Ni_{Cd}) is closer to the $y = x$ line than the charge on the S atoms (Ni_S), showing preferential Ni−Cd bonding for Ni clusters. Most other metal clusters show a preferential bonding with S atoms, where the Pd_S, Pt_S, and Au_S are higher in magnitude and closer to the $y = x$ line than Pd_{Cd}, Pt_{Cd}, and Au_{Cd}, respectively. These results are consistent from what one would expect from Figure 2 for single-atom cases.

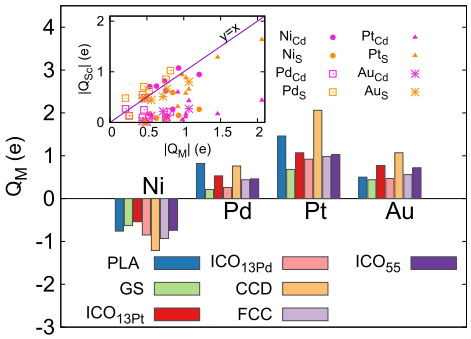

Figure 7. Bar plots showing the sum of Bader charge differences for deposited clusters. The inset uses the sum of Bader charge differences for the substrate atoms, where the absolute values of Q_{Cd} and Q_S (as $|Q_{Sc}|$) are plotted against the absolute value of the Q_M represented in the main panel.

3.3.2. E_{adh} vs BE. Figure 8 shows the variation of E_{adh} as a function of a cluster's freestanding BE. The E_{adh} includes the chemical interaction energy as well the cluster deformation energy over the substrate. The point on the extreme left corresponds to the E_{adh} of the single-atom GS cases of Figure 1. Moving toward the right corresponds to 13-atom and 55-atom clusters, respectively. For each cluster, we have plotted

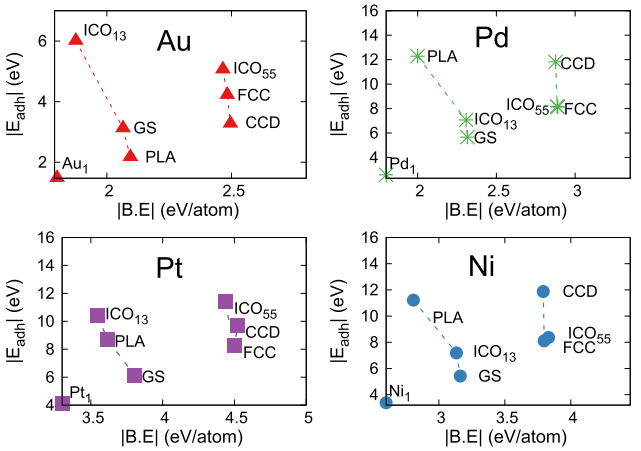

Figure 8. Absolute cluster adhesion energy ($|E_{adh}|$) on the substrate as a function of its freestanding absolute binding energy (|BE|).

the configuration with the highest E_{adh}. This also holds for the two types of adsorbed configurations of ICO_{13} clusters (ICO_{Pd} and ICO_{Pt}), where we have chosen the most stable adsorption configurations for the particular metal case. First, the order of the single-atom E_{adh}, $E_{adh}^{Pt} > E_{adh}^{Ni} > E_{adh}^{Pd} > E_{adh}^{Au}$, is inverse to the order bulk BE of the metal (shown in Figure 3). The E_{adh} values of Au clusters are significantly lower than those of other metals, owing to its weakly interacting d-bands. Second, it is not necessary that as the cluster atomicity increases, the E_{adh} would increase. ICO_{13} cluster of Au and Pt and PLA cluster of Ni and Pd are such examples, whose E_{adh} values exceed those of some of the 55-atom clusters. Third, through the chemical interaction contribution, it only implicitly depends on the clusters' interfacial area. ICO_{13} and ICO_{55} clusters of Au and Pt illustrate the case with high E_{adh}, but low interfacial area. In such cases, diffusion-assisted bonding and surface reactivity of the cluster can be expected to dominate in determining the E_{adh}. Fourth, for the 13-atom clusters of all of the metals, the function shows a negative slope, hence corroborating the expectation that the more stable a freestanding cluster, the lesser will be its reactivity with the substrate. However, this correlation can be expected to hold only for small clusters where most of the atoms are exposed to substrate interaction. For the 55-atom clusters, there is only an approximate negative correlation of E_{adh} with BE. This is not surprising since only a few metal atoms at the deposition facet lead to substrate interaction, and would not strictly be correlated with the BE per atom. Nonetheless, the Au clusters that interact weakly with the surface show a clear negative correlation even for 55-atom clusters.

3.4. Metallicity and Schottky Barrier Height. Finally, we examined the band gap regions of the M−Sc interfaces and determined if the resulting interfaces were metallized or retained the semiconducting feature of the substrate. We performed a single-point calculation with a high k-mesh (9−10 irreducible k-points) for the interface geometries. The cases that exhibit distinct change in occupation of bands, over different k-points, are regarded as clearly metallic. The cases with less than 15 meV of HOMO−LUMO gap were considered almost metallic. For other cases, we calculated the HOMO−LUMO gaps for the spin-up and spin-down channels separately. In Table 2, we list the smallest of the two gaps and mark the cases which are metallic interfaces.

DOI: 10.1021/acs.jpcc.9b02319
J. Phys. Chem. C 2019, 123, 9298−9310

First, comparing with the HOMO−LUMO gaps in Table 1 for the isolated clusters, we observe that most of the 13-atom interfaces are semiconducting, wherein the HOMO−LUMO gaps of some of the interfaces increased or decreased (in comparison to gas phase), owing to the physical deformation or new bonding states with the substrate. Au-PLA shows a clear change in occupation for one of the bands, while the Ni-GS case has a gap as small as 19 meV. With a single-point calculation of the deformed metal cluster derived from an interface calculation, we observe that the gap for an isolated cluster remains unchanged within 10 meV of the gap (from Table 2) for the pristine cluster. This is because the cluster network mostly remains intact as shown in Figure 5. The transition of Au-PLA to metallicity, when deposited, occurs due to the new chemical bonding states. In distinction from this, out of the total decrease of HOMO−LUMO gap of 121 meV, between the pristine Ni-GS cluster and its interface with the CdS, physical deformation contributes to ∼60 meV reduction in the gap (estimated by single-point calculation of the deformed cluster). The remaining gap reduction is compensated by the chemical states emerging in the gap of the substrate. For Au-PLA, these midgap chemical states are shown in Figure 9a, where the layer-resolved DOS is shown for

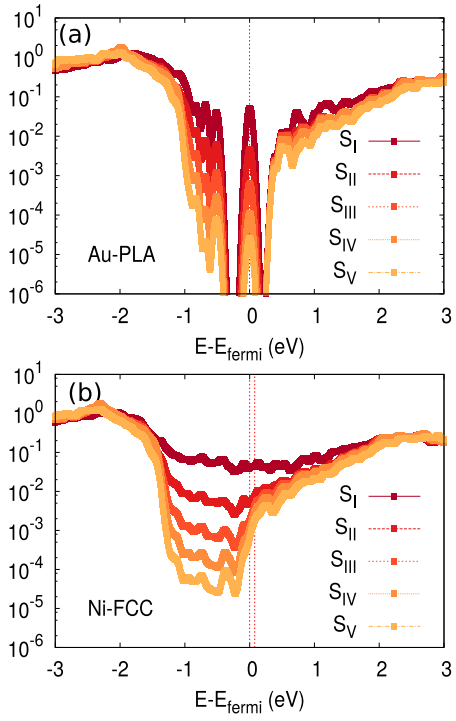

Figure 9. (a, b) Layer-resolved DOS of the substrate S atoms, for Au-PLA and Ni-FCC cluster depositions, respectively. S_I refers to the topmost layer of anions, and higher numbers to subsequent subsurface layers. The dashed lines in (b) represent the Fermi level and the conduction band edge.

the substrate S atoms. As the number of bands crossing the Fermi level is not large (only one), we do not observe a complete closing of the gap region.

Second, several of the 55-atom clusters that exhibit gaps in the gas phase turn the interface metallic (or almost metallic) for all of the metals except Pt. For Pt_{55} clusters, although the transferred charge and E_{adh} are higher than those of other metals, the new chemical states do not result in significant reduction of the gaps. This may indicate that the Pt−S bonds result in chemical states slightly deeper than the valence band edge.

Third, we also studied the SOC effect for deposited Au clusters with a single-point, dense *k*-mesh with 9−10 irreducible *k*-points. The effect of including SOC for Au clusters is similar to that observed in the gas phase, where the HOMO−LUMO gap reduces, in general. All of the Au clusters, except Au-PLA, strictly show this trend. Nonetheless, the Au-PLA gap with SOC is only 8 meV, in comparison to metallized surface without SOC. The marked influence of including SOC for ICO_{13} is also seen for the deposited ICO_{13} cases, similar to the gas phase shown in Figure S8.

For the depositions that showed a negligibly small HOMO−LUMO gap or a clearly metallized interface, we calculated the n-type Schottky barrier heights (SBHs), i.e., $E_{CBM} - E_F$, shown in the bottom of Table 2. For this, we use the electrostatic average of the deep bulklike atomic layers (E_{bulk}) of the substrate slab, as a reference to obtain E_{CBM}. That is, the E_{bulk} and E_F values are calculated from each deposited case, while the difference between the E_{CBM} and E_{bulk} values is taken from a pristine CdS slab. This is done for all of the 55-atom clusters, but not for the Pt clusters, as the latter do not close the band gap in the cluster types and sizes examined in this study.

In the bottom of Table 2, we observe that there is no SOC effect on the SBH Au_{55} clusters. This is expected as both the E_{bulk} and E_F are not expected to significantly vary by SOC effects. Of the 12 clusters, only Ni-FCC shows SBH less than 10 meV. We regard it as an example of an ohmic contact. The layer-resolved DOS is shown for Ni-FCC in Figure 9b, where the energy levels are broadened with a Gaussian width of 50 meV. The closing of the gap seen in Figure 9b is representative of the 55-atom depositions of Ni, Pd, and Au.

4. CONCLUSIONS

In this work, we have highlighted the bonding similarities and differences among the metal−CdS($10\bar{1}0$) interfaces of Ni, Pd, Pt, and Au. The Ni−Cd bonding primarily leads to the depletion of electronic charge at the metal end. Among the metals in the Ni group, this bonding behavior decreases from 3d → 4d → 5d (from Ni → Pd → Pt). In comparison to the Ni interface, the induced dipole is opposite in polarity for Pd, Pt, and Au. Single-atom Pt as well as subnanometer-sized Pt depositions exhibit larger charge transfers than other metals. Similar to gas-phase trends, clusters of Ni and Pd tend to remain compact while reacting with the substrate, whereas Pt and Au clusters lead to more disordered interfaces. The HOMO−LUMO gaps for all of the 55-atom metal clusters considered here show a reduction upon deposition over the CdS surface, except for Pt. The Pt clusters and their deposited interfaces could exhibit metallic behavior for larger cluster atomicity. Spin−orbit coupling (SOC) effects examined for Au depositions further lead to gap reduction. However, SOC does not affect the charge transfer or the Schottky barrier height (SBH) of the deposited clusters. The SBHs indicated for subnanometer clusters are much lower than those indicated for macroscopic samples studied in experimental reports. One of the 55-atom clusters shows an Ohmic contact. No clear intermetallic trends could be observed for the SBHs. Overall, the present work shows that the electronic structure of these subnanometer interfaces may lead to emergent metallicity at the interface, owing to the interfacial bonding, for interaction between semiconductor gas-phase clusters and the semi-

DOI: 10.1021/acs.jpcc.9b02319
J. Phys. Chem. C 2019, 123, 9298−9310

conductor CdS substrate. Trends observed for single-atom depositions (such as the Ni−Cd bonding complex identified in this work) are largely extendable to subnanometer 13-atom and 55-atom clusters. The present work underlines similarities across subnanometer clusters and the intermetallic differences at these CdS−M interfaces, which are characterized by the typical electronic nature of the interfaces and the resulting charge transfers. This naturally forms the fundamental difference in the chemical environment provided by these interfaces, whose effect on reaction intermediates will be a topic of further study.

■ ASSOCIATED CONTENT

Supporting Information

The Supporting Information is available free of charge on the ACS Publications website at DOI: 10.1021/acs.jpcc.9b02319.

Additional (metastable) deposited configurations, analysis of (partial) density of states and charge densities, charge transfers, overview of all considered clusters, and spin polarization of the clusters (PDF)

Structure files of single-atom and cluster deposition configurations (ZIP)

■ AUTHOR INFORMATION

Corresponding Author

*E-mail: M.A.vanHuis@uu.nl.

ORCID

M. A. van Huis: 0000-0002-8039-2256

Notes

The authors declare no competing financial interest.

■ ACKNOWLEDGMENTS

M.A.v.H. acknowledges support from the European Research Council (ERC Consolidator Grant No. 683076 NANO-INSITU). This work is part of the Industrial Partnership Programme "Computational Sciences for Energy Research" (Grant No. 13CSER067) of the Netherlands Organization for Scientific Research NWO-i. This research program was co-financed by Shell Global Solutions International B.V.

■ REFERENCES

(1) Ben-Shahar, Y.; Banin, U. Hybrid Semiconductor-Metal Nanorods as Photocatalysts. *Top. Curr. Chem.* **2016**, *374*, 54.

(2) Kalisman, P.; Nakibli, Y.; Amirav, L. Perfect Photon-to-Hydrogen Conversion Efficiency. *Nano Lett.* **2016**, *16*, 1776−1781.

(3) Banin, U.; Ben-Shahar, Y.; Vinokurov, K. Hybrid Semiconductor-Metal Nanoparticles: From Architecture to Function. *Chem. Mater.* **2014**, *26*, 97−110.

(4) Elmalem, E.; Saunders, A. E.; Costi, R.; Salant, A.; Banin, U. Growth of Photocatalytic CdSe-Pt Nanorods and Nanonets. *Adv. Mater.* **2008**, *20*, 4312−4317.

(5) Amirav, L.; Alivisatos, A. P. Photocatalytic Hydrogen Production with Tunable Nanorod Heterostructures. *J. Phys. Chem. Lett.* **2010**, *1*, 1051−1054.

(6) Bao, N.; Shen, L.; Takata, T.; Domen, K. Self-Templated Synthesis of Nanoporous CdS Nanostructures for Highly Efficient Photocatalytic Hydrogen Production under Visible Light. *Chem. Mater.* **2008**, *20*, 110−117.

(7) Vaneski, A.; Schneider, J.; Susha, A. S.; Rogach, A. L. Colloidal hybrid heterostructures based on II-VI semiconductor nanocrystals for photocatalytic hydrogen generation. *J. Photochem. Photobiol., C* **2014**, *19*, 52−61.

(8) Berr, M.; Vaneski, A.; Susha, A. S.; Rodríguez-Fernández, J.; Döblinger, M.; Jäckel, F.; Rogach, A. L.; Feldmann, J. Colloidal CdS nanorods decorated with subnanometer sized Pt clusters for photocatalytic hydrogen generation. *Appl. Phys. Lett.* **2010**, *97*, No. 093108.

(9) Schweinberger, F. F.; Berr, M. J.; Döblinger, M.; Wolff, C.; Sanwald, K. E.; Crampton, A. S.; Ridge, C. J.; Jäckel, F.; Feldmann, J.; Tschurl, M.; Heiz, U. Cluster Size Effects in the Photocatalytic Hydrogen Evolution Reaction. *J. Am. Chem. Soc.* **2013**, *135*, 13262−13265.

(10) Ben-Shahar, Y.; Scotognella, F.; Kriegel, I.; Moretti, L.; Cerullo, G.; Rabani, E.; Banin, U. Optimal metal domain size for photocatalysis with hybrid semiconductor-metal nanorods. *Nat. Commun.* **2016**, *7*, No. 10413.

(11) Karakus, M.; Sung, Y.; Wang, H. I.; Mics, Z.; Char, K.; Bonn, M.; Cánovas, E. Correlating Carrier Dynamics and Photocatalytic Hydrogen Generation in Pt Decorated CdSe Tetrapods as a Function of Cocatalyst Size. *J. Phys. Chem. C* **2017**, *121*, 13070−13077.

(12) Nakibli, Y.; Mazal, Y.; Dubi, Y.; Wächtler, M.; Amirav, L. Size Matters: Cocatalyst Size Effect on Charge Transfer and Photocatalytic Activity. *Nano Lett.* **2018**, *18*, 357−364.

(13) Dulub, O.; Diebold, U.; Kresse, G. Novel Stabilization Mechanism on Polar Surfaces: ZnO(0001)-Zn. *Phys. Rev. Lett.* **2003**, *90*, No. 016102.

(14) Mora-Fonz, D.; Lazauskas, T.; Farrow, M. R.; Catlow, C. R. A.; Woodley, S. M.; Sokol, A. A. Why Are Polar Surfaces of ZnO Stable? *Chem. Mater.* **2017**, *29*, 5306−5320.

(15) Menagen, G.; Macdonald, J. E.; Shemesh, Y.; Popov, I.; Banin, U. Au Growth on Semiconductor Nanorods: Photoinduced versus Thermal Growth Mechanisms. *J. Am. Chem. Soc.* **2009**, *131*, 17406−17411.

(16) Yin, Y.; Alivisatos, A. P. Colloidal nanocrystal synthesis and the organic-inorganic interface. *Nature* **2005**, *437*, 664.

(17) Naskar, S.; Lübkemann, F.; Hamid, S.; Freytag, A.; Wolf, A.; Koch, J.; Ivanova, I.; Pfnür, H.; Dorfs, D.; Bahnemann, D. W.; Bigall, N. C. Synthesis of Ternary and Quaternary Au and Pt Decorated CdSe/CdS Heteronanoplatelets with Controllable Morphology. *Adv. Funct. Mater.* **2017**, *27*, No. 1604685.

(18) Sung, Y.; Lim, J.; Koh, J. H.; Hill, L. J.; Min, B. K.; Pyun, J.; Char, K. Uniform decoration of Pt nanoparticles on well-defined CdSe tetrapods and the effect of their Pt cluster size on photocatalytic H2 generation. *CrystEngComm* **2015**, *17*, 8423−8427.

(19) Rudolf, H. Effective coordination numbers (ECoN) and mean fictive ionic radii (MEFIR). *Z. Kristallogr. − Cryst. Mater.* **1979**, *150*, 23−52.

(20) Piotrowski, M. J.; Piquini, P.; Da Silva, J. L. F. Density functional theory investigation of 3*d*, 4*d*, and 5*d*13-atom metal clusters. *Phys. Rev. B* **2010**, *81*, No. 155446.

(21) Calle-Vallejo, F.; Loffreda, D.; Koper, M. T. M.; Sautet, P. Introducing structural sensitivity into adsorption-energy scaling relations by means of coordination numbers. *Nat. Chem.* **2015**, *7*, 403.

(22) Hohenberg, P.; Kohn, W. Inhomogeneous Electron Gas. *Phys. Rev.* **1964**, *136*, B864−B871.

(23) Kohn, W.; Sham, L. J. Self-Consistent Equations Including Exchange and Correlation Effects. *Phys. Rev.* **1965**, *140*, A1133−A1138.

(24) Kresse, G.; Furthmüller, J. Efficiency of ab-initio total energy calculations for metals and semiconductors using a plane-wave basis set. *Comput. Mater. Sci.* **1996**, *6*, 15−50.

(25) Kresse, G.; Furthmúller, J. Efficient iterative schemes for *ab initio* total-energy calculations using a plane-wave basis set. *Phys. Rev. B* **1996**, *54*, 11169−11186.

(26) Blöchl, P. E. Projector augmented-wave method. *Phys. Rev. B* **1994**, *50*, 17953−17979.

(27) Kresse, G.; Joubert, D. From ultrasoft pseudopotentials to the projector augmented-wave method. *Phys. Rev. B* **1999**, *59*, 1758−1775.

(28) Perdew, J. P.; Burke, K.; Ernzerhof, M. Generalized Gradient Approximation Made Simple. *Phys. Rev. Lett.* **1996**, *77*, 3865−3868.

DOI: 10.1021/acs.jpcc.9b02319
J. Phys. Chem. C 2019, 123, 9298−9310

(29) Sze, S. M. *Physics of Semiconductor Devices*; John Wiley & Sons, Ltd., 1981.
(30) Adachi, S. *Properties of Group-IV, III−V and II−VI Semiconductors*; John Wiley & Sons, Ltd., 2005; pp 1−21.
(31) Bengtsson, L. Dipole correction for surface supercell calculations. *Phys. Rev. B* **1999**, *59*, 12301−12304.
(32) Neugebauer, J.; Scheffler, M. Adsorbate-substrate and adsorbate-adsorbate interactions of Na and K adlayers on Al(111). *Phys. Rev. B* **1992**, *46*, 16067−16080.
(33) Van de Walle, C. G.; Martin, R. M. Theoretical study of band offsets at semiconductor interfaces. *Phys. Rev. B* **1987**, *35*, 8154−8165.
(34) Hinuma, Y.; Gruneis, A.; Kresse, G.; Oba, F. Band alignment of semiconductors from density-functional theory and many-body perturbation theory. *Phys. Rev. B* **2014**, *90*, No. 155405.
(35) Jiang, H.; Shen, Y.-C. Ionization potentials of semiconductors from first-principles. *J. Chem. Phys.* **2013**, *139*, No. 164114.
(36) Stevanović, V.; Lany, S.; Ginley, D. S.; Tumas, W.; Zunger, A. Assessing capability of semiconductors to split water using ionization potentials and electron affinities only. *Phys. Chem. Chem. Phys.* **2014**, *16*, 3706−3714.
(37) Chen, W.; Pasquarello, A. Band-edge positions in GW: Effects of starting point and self-consistency. *Phys. Rev. B* **2014**, *90*, No. 165133.
(38) Swank, R. K. Surface Properties of II-VI Compounds. *Phys. Rev.* **1967**, *153*, 844−849.
(39) Anisimov, V. I.; Aryasetiawan, F.; Lichtenstein, A. I. First-principles calculations of the electronic structure and spectra of strongly correlated systems: the LDA + U method. *J. Phys.: Condens. Matter* **1997**, *9*, 767.
(40) Dudarev, S. L.; Botton, G. A.; Savrasov, S. Y.; Humphreys, C. J.; Sutton, A. P. Electron-energy-loss spectra and the structural stability of nickel oxide: An LSDA+U study. *Phys. Rev. B* **1998**, *57*, 1505−1509.
(41) Cheng, N.; Stambula, S.; Wang, D.; Banis, M. N.; Liu, J.; Riese, A.; Xiao, B.; Li, R.; Sham, T.-K.; Liu, L.-M.; Botton, G. A.; Sun, X. Platinum single-atom and cluster catalysis of the hydrogen evolution reaction. *Nat. Commun.* **2016**, *7*, No. 13638.
(42) Liu, L.; Corma, A. Metal Catalysts for Heterogeneous Catalysis: From Single Atoms to Nanoclusters and Nanoparticles. *Chem. Rev.* **2018**, *118*, 4981−5079.
(43) Schwarz, W. H. E. The Full Story of the Electron Configurations of the Transition Elements. *J. Chem. Educ.* **2010**, *87*, 444−448.
(44) Xiong, S.; Isaacs, E. B.; Li, Y. Adsorption Characteristics and Size/Shape Dependence of Pt Clusters on the CdS Surface. *J. Phys. Chem. C* **2015**, *119*, 4834−4842.
(45) Blöchl, P. E.; Jepsen, O.; Andersen, O. K. Improved tetrahedron method for Brillouin-zone integrations. *Phys. Rev. B* **1994**, *49*, 16223−16233.
(46) Henkelman, G.; Arnaldsson, A.; Jónsson, H. A fast and robust algorithm for Bader decomposition of charge density. *Comput. Mater. Sci.* **2006**, *36*, 354−360.
(47) Huang, W.; Ji, M.; Dong, C.-D.; Gu, X.; Wang, L.-M.; Gong, X. G.; Wang, L.-S. Relativistic Effects and the Unique Low-Symmetry Structures of Gold Nanoclusters. *ACS Nano* **2008**, *2*, 897−904.
(48) Chou, J. P.; Hsing, C. R.; Wei, C. M.; Cheng, C.; Chang, C. M. Ab initio random structure search for 13-atom clusters of fcc elements. *J. Phys.: Condens. Matter* **2013**, *25*, No. 125305.
(49) Piotrowski, M. J.; Ungureanu, C. G.; Tereshchuk, P.; Batista, K. E. A.; Chaves, A. S.; Guedes-Sobrinho, D.; Da Silva, J. L. F. Theoretical Study of the Structural, Energetic, and Electronic Properties of 55-Atom Metal Nanoclusters: A DFT Investigation within van der Waals Corrections, Spin-Orbit Coupling, and PBE+U of 42 Metal Systems. *J. Phys. Chem. C* **2016**, *120*, 28844−28856.
(50) Chaves, A. S.; Piotrowski, M. J.; Da Silva, J. L. F. Evolution of the structural, energetic, and electronic properties of the 3d, 4d, and 5d transition-metal clusters (30 TMn systems for n = 2−15): a density functional theory investigation. *Phys. Chem. Chem. Phys.* **2017**, *19*, 15484−15502.
(51) Harrison, W. *Electronic Structure and Properties of the Solid*; W. H. Freeman and Company, 1980.
(52) Johansson, M. P.; Warnke, I.; Le, A.; Furche, F. At What Size Do Neutral Gold Clusters Turn Three-Dimensional? *J. Phys. Chem. C* **2014**, *118*, 29370−29377.
(53) Pelzer, A. W.; Jellinek, J.; Jackson, K. A. H2 Reactions on Palladium Clusters. *J. Phys. Chem. A* **2013**, *117*, 10407−10415.
(54) Sun, Y.; Zhang, M.; Fournier, R. Periodic trends in the geometric structures of 13-atom metal clusters. *Phys. Rev. B* **2008**, *77*, No. 075435.
(55) Munoz, F.; Varas, A.; Rogan, J.; Valdivia, J. A.; Kiwi, M. Au13-nAgn clusters: a remarkably simple trend. *Phys. Chem. Chem. Phys.* **2015**, *17*, 30492−30498.
(56) Doye, J. P. K. Identifying structural patterns in disordered metal clusters. *Phys. Rev. B* **2003**, No. 195418.
(57) Furche, F.; Ahlrichs, R.; Weis, P.; Jacob, C.; Gilb, S.; Bierweiler, T.; Kappes, M. M. The structures of small gold cluster anions as determined by a combination of ion mobility measurements and density functional calculations. *J. Chem. Phys.* **2002**, *117*, 6982−6990.
(58) Nayak, S. K.; Khanna, S. N.; Rao, B. K.; Jena, P. Physics of Nickel Clusters: Energetics and Equilibrium Geometries. *J. Phys. Chem. A* **1997**, *101*, 1072−1080.
(59) Futschek, T.; Marsman, M.; Hafner, J. Structural and magnetic isomers of small Pd and Rh clusters: an ab initio density functional study. *J. Phys.: Condens. Matter* **2005**, *17*, 5927.
(60) Futschek, T.; Hafner, J.; Marsman, M. Stable structural and magnetic isomers of small transition-metal clusters from the Ni group: an ab initio density-functional study. *J. Phys.: Condens. Matter* **2006**, *18*, 9703.
(61) Johansson, M. P.; Lechtken, A.; Schooss, D.; Kappes, M. M.; Furche, F. 2D-3D transition of gold cluster anions resolved. *Phys. Rev. A* **2008**, *77*, No. 053202.
(62) Chou, J. P.; Chen, H. Y. T.; Hsing, C. R.; Chang, C. M.; Cheng, C.; Wei, C. M. 13-atom metallic clusters studied by density functional theory: Dependence on exchange-correlation approximations and pseudopotentials. *Phys. Rev. B* **2009**, *80*, No. 165412.
(63) Häkkinen, H.; Moseler, M.; Landman, U. Bonding in Cu, Ag, and Au Clusters: Relativistic Effects, Trends, and Surprises. *Phys. Rev. Lett.* **2002**, *89*, No. 033401.
(64) Batista, K. E. A.; Piotrowski, M. J.; Chaves, A. S.; Da Silva, J. L. F. A theoretical investigation of the structural and electronic properties of 55-atom nanoclusters: The examples of Y-Tc and Pt. *J. Chem. Phys.* **2016**, *144*, No. 054310.

DOI: 10.1021/acs.jpcc.9b02319
J. Phys. Chem. C 2019, 123, 9298−9310